# 1. Computing hemodynamics in the Circle of Willis

By Kristian Valen-Sendstad, Kent-Andre Mardal, and Anders Logg

Computational fluid dynamics (CFD) is a tool with great potential in medicine. Using traditional engineering techniques, one may compute, e.g., the blood flow in arteries and the resulting stress on the vessel wall to understand, treat, and prevent various cardiovascular diseases. This chapter is devoted to the computation of blood flow in large cerebral arteries and its role in the development and rupture of aneurysms. We discuss the process from generating geometries from medical imaging data to performing patient-specific simulations of hemodynamics in FEniCS. Specifically, we present three different applications: simulations related to a recently published study [16] concerning gender differences in cerebral arteries, a study of the carotid arteries of a canine with an induced aneurysm [13], and a study of the blood flow in a healthy Circle of Willis, where patient-specific velocity measurements are compared with a model for the peripheral resistance.

## 1.1 Medical background

Stroke is a leading cause of death in the developed part of the world [7], and mortality rates could increase dramatically in the years to come [20]. Stroke is caused by an insufficient supply of blood to parts of the brain. There are mainly two different types of strokes, ischemia caused by obstructions in the blood vessels, and subarachnoid hemorrhage caused by the rupture of one or more aneurysms [11]. Aneurysms typically develop in or near the so-called Circle of Willis (CoW), which is an arterial network of vessels at the base of the brain. The function of this circle is believed to be to ensure a robust and redundant system in the sense that the brain will receive a sufficient amount of blood even if one of the vessels is occluded or under-developed. This network connects the (internal) carotid arteries and the vertebral arteries into a circle-like structure. This network is the main supplier of blood to the brain. Figure 1.1 shows the circle as typically depicted in textbooks and Figure 1.2 shows a circle with multiple aneurysms. The Figure 1.2 shows the brain as seen from below where the left part of the brain is removed. Blood enters the circle through the Internal Carotid Arteries (ICAs), which is located at the front of the neck and the Vertebral Arteries (VAs) located in the back of the neck. The VAs join in the Basilar Artery (BA), and blood leaves the circle in the front through the Anterior Cerebral Arteries (ACA), in the back through the Posterior Cerebral Arteries (PCA), and at the sides through the Middle Cerebral Arteries (MCA). A patient-specific circle, the one used in Section 1.5, is shown in Figure 1.3.

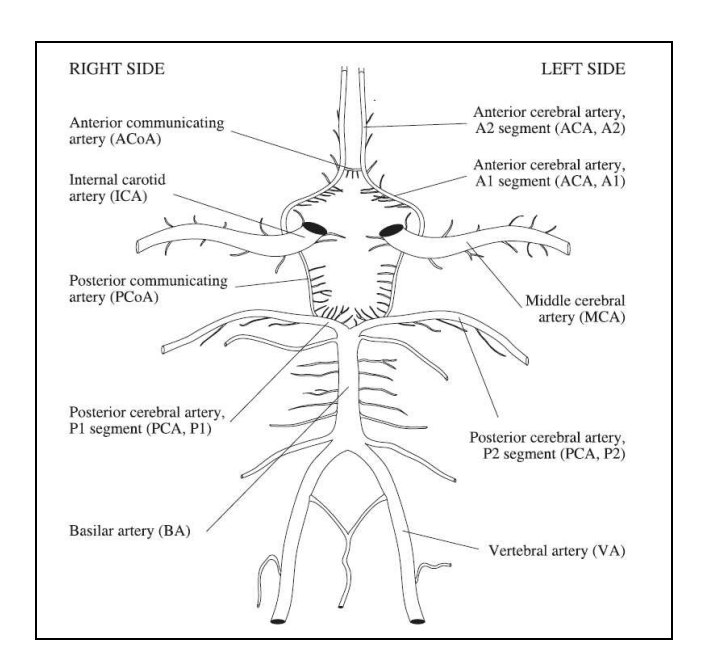


Figure 1.1: Illustration of the Circle of Willis with abbreviations used in this chapter.

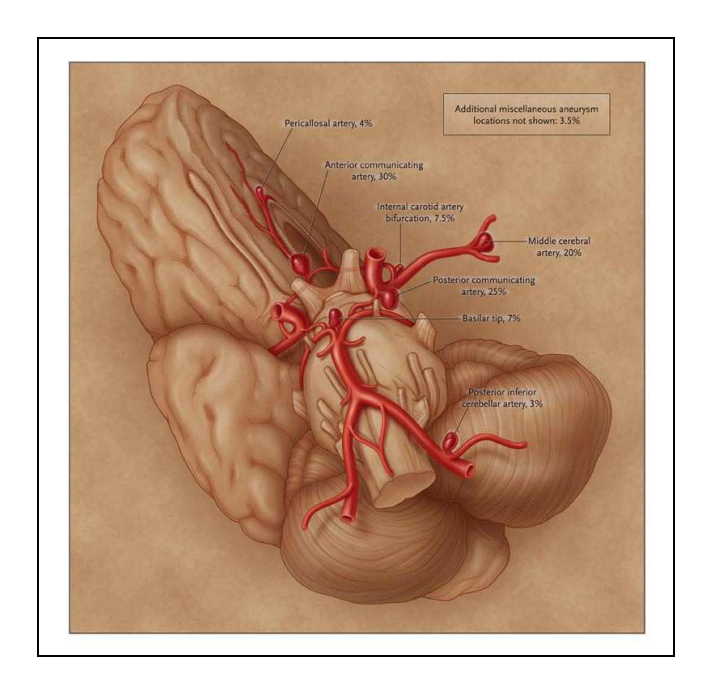


Figure 1.2: An illustration of the Circle of Willis with multiple aneurysms.

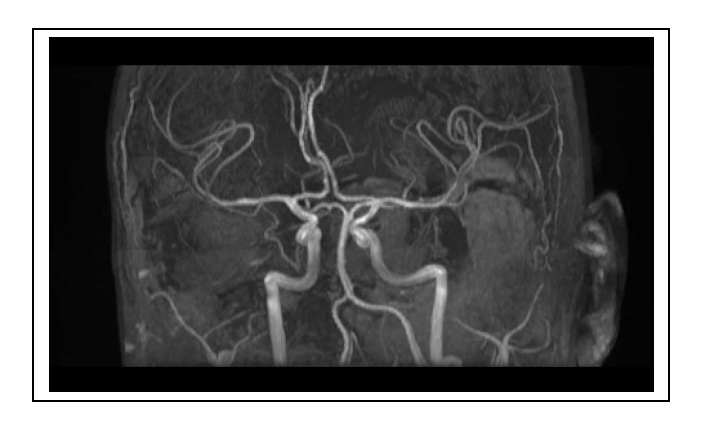


Figure 1.3: A patient-specific Circle of Willis.

#### ▶ Editor note: *Check copyright for Figures 1.1 and 1.2.*

Aneurysms are relatively common, as many as 1–6% of the population develop aneurysms during a lifetime [25]. Unfortunately, aneurysms also rupture at a relatively early age. The average age of rupture is 52 years [11]. An intracranial aneurysm is a dilatation of the blood vessel wall, and the reason for initialization, growth, and rupture of aneurysms are largely unknown. What is known is that increased wall shear stress (WSS) affects vascular endothelial cells turnover [4], that aneurysms may grow in the direction of low wall shear stress [2], and that flow pattern and impingement zones affect the possibility of rupture [3]. The vessel wall clearly responds to mechanical stimuli and this is the reason why wall shear stress is of special importance when trying to understand the pathogenesis of intracranial aneurysms. It is also known that the cerebral arteries lack perivascular support and the walls are relatively thin relative to the rest of the intracranial vasculature [11, 22]. Furthermore, the anatomy of cerebral vessels varies greatly. Only around 50% of the general population have a complete circle; the rest either have under-developed vessels or the vessels are missing completely [9]. Both gender, ethnicity, and lifestyle have shown to be of importance [19, 17, 14].

#### 1.2 Preliminaries

#### 1.2.1 Stress calculation

We noted above that wall shear stress is of importance in computational hemodynamics. In Figure 1.2.1, we demonstrate how to compute stresses in FEniCS from a computed velocity field u and pressure field p. We start from the definition of the stress tensor  $\sigma(u,p)=2\nu\varepsilon(u)-pI$ , where the  $\varepsilon(u)=\frac{1}{2}(\nabla u+\nabla u^T)$  is the symmetric gradient. Then, the normal and tangential components of the stress are computed, where the tangential component is computed by subtracting the normal component from the traction  $T=-\sigma\cdot n$ . Here, n is the inward-pointing unit normal from the vessel wall. In the code, n is the outward-pointing unit normal. To compute the shear and normal stresses as fields over the mesh, we test the stresses against piecewise constant test functions scaled by the inverse area of each facet. We thus obtain a piecewise constant representation of the stresses which on each cell is equal to the average stress on that cell.

```
# Compute stress tensor
sigma = 2*nu*epsilon(u) - p*Identity(len(u))
# Compute surface traction
n = FacetNormal(mesh)
T = -sigma*n
# Compute normal and tangential components
Tn = inner(T, n) # scalar-valued
Tt = T - Tn*n
                # vector-valued
# Piecewise constant test functions
scalar = FunctionSpace(mesh, "DG", 0)
vector = VectorFunctionSpace(mesh, "DG", 0)
v = TestFunction(scalar)
w = TestFunction(vector)
# Assemble piecewise constant functions for stress
normal_stress = Function(scalar)
shear_stress = Function(vector)
Ln = (1 / FacetArea(mesh))*v*Tn*ds
Lt = (1 / FacetArea(mesh))*inner(w, Ft)*ds
assemble(Ln, tensor=normal_stress.vector())
assemble(Lt, tensor=shear_stress.vector())
```

Figure 1.4: Computing normal and shear stresses from computed velocity and pressure fields u and p.

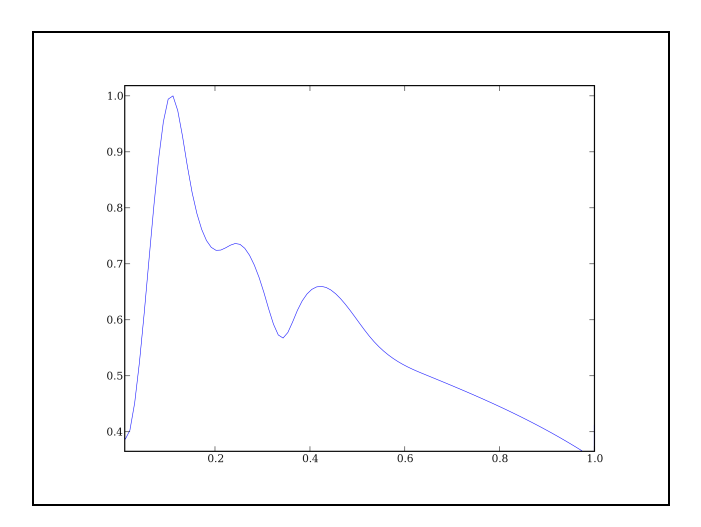


Figure 1.5: Nondimensionalized ICA inlet velocity profile.

#### 1.2.2 Boundary conditions

For transient inlet boundary conditions, one option is to apply velocity waveform data in the Internal Carotid Artery (ICA) from Ford et al. [8], where the average velocity was measured for seventeen young patients at rest. The nondimensionalized velocity is illustrated in Figure 1.5. The inlet velocity profile is easy to measure through the ICA or the Vertebral Arteries (VA) using transcranial Doppler and patient-specific velocity measurements are possible to apply, such as in the CoW study in Section 1.5.

Further into the brain, the flow is divided into branches several times, which makes the outflow difficult to measure, both because of the thickness of the cranium and the decreasing size of the vessels. The effect of outflow boundary conditions in a complex network of blood vessels, such as in the Circle of Willis, is important to the flow division and wall shear stress.

The simplest way to describe the outflow is by applying a zero traction boundary condition at the outflow. However, the flow division in a bifurcation is dependent on the downstream vasculature, and the zero traction boundary condition does not capture this very well. Therefore, to model the the peripheral resistance, a resistance model may be used for the pressure, while a Neumann  $(\partial u/\partial n = 0)$  is applied to the velocity. The value of the resistance boundary condition is proportional to the flow, that is, the pressure at the outlet is modeled as,

$$p = p_0 + R = p_0 + C \int_{\Gamma} (u \cdot n) \, dS,$$
 (1.1)

where the resistance coefficient C was set according to Table 1.1,  $p_0$  is the mean intracranial arterial pressure (85 mmHg) which is applied to the inlet and u is the velocity. The coefficients in Table 1.1 are from [1] and show a clear relation between the diameter of the vessel and the resistance coefficient. The implementation is shown in Figure 1.6.

The effect of the resistance boundary condition may bee seen in Figure 1.7 where the mass flux over two outlets in the canine geometry in Section 1.4 is calculated using both zero traction and a resistance boundary condition. The resulting flow division is clearly more evenly distributed (colored in red) between the daughter vessels, which intuitively also makes sense since the vessels reconnect further downstream. The method requires a

| Artery                         | $C \left[ 10^9 \text{Pa} \cdot \text{s} \cdot \text{m}^{-3} \right]$ | Radius[mm] |
|--------------------------------|--|------------|
| Thoracic Aorta                 | 0.18   | 9.99       |
| External Carotid Artery        | 5.43   | 1.50       |
| Middle Cerebral Artery         | 5.97   | 1.43       |
| Anterior Communicating Artery  | 8.48   | 1.20       |
| Posterior Communicating Artery | 11.08  | 1.05       |

Table 1.1: Summary of resistance boundary conditions coefficient *C* for arteries of varying size.

```
# Outflow boundary value for pressure
def OutflowBoundaryValue(self, i):
    u = self.problem.u
    n = FacetNormal(self.problem.mesh)
    flux = dot(u, n)*ds(i)
    Q = assemble(flux, exterior_facet_domains=self.problem.sub_domains)
    C = 5.97*10**(-3)
    p0 = 11332.0*10**(-6) # Bloodpressure, 85 mmHg in Pa
    R = (C*Q + p0)*975.6097560975611
    print "Computed resistance on side ", i, " is ", R, " the flux is ", Q
    print "Constant pressure is ", p0, " and dynamic resistance is ", C*Q
    return R
```

Figure 1.6: Calculation of outflow boundary value for pressure.

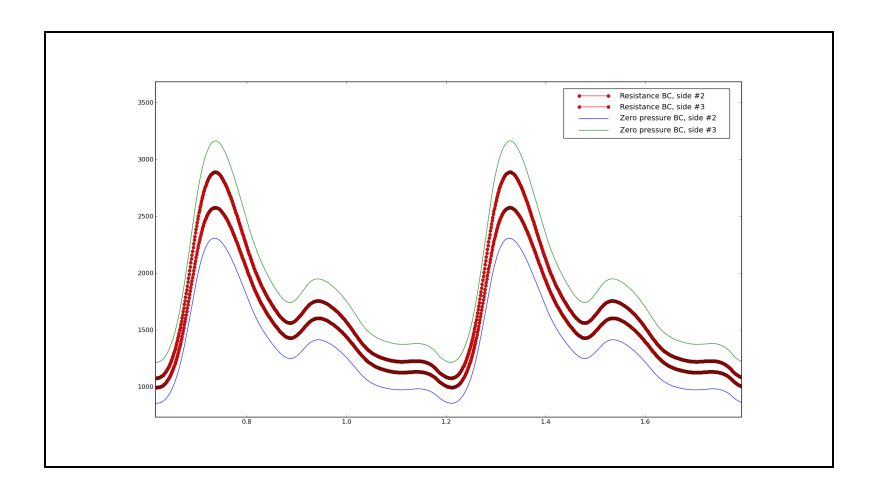


Figure 1.7: Figure showing the difference of outflow flux when a resistance boundary condition (as described in section 1.2.2) is applied versus zero traction.

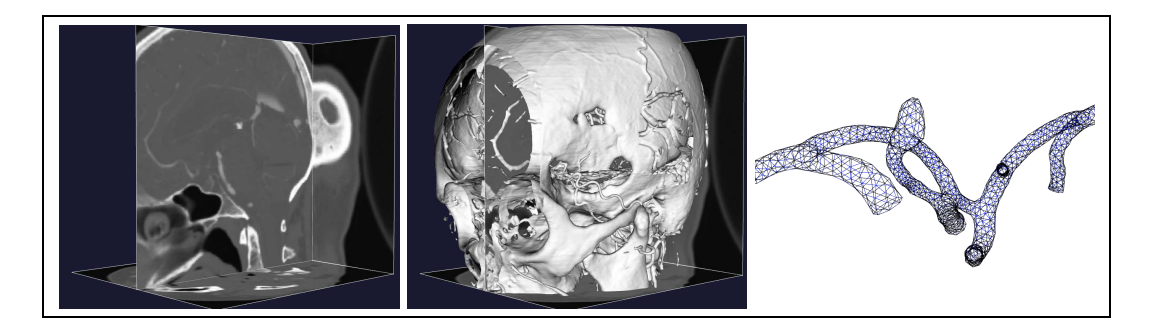


Figure 1.8: Image segmentation process; from MRI to mesh.

iteration over a few cardiac cycles in order to converge.

#### 1.2.3 Anatomical modeling

Segmentation of patient-specific geometries are based upon CTA or MRA images. A stack of 2D images is used as input to the Vascular Modeling Toolkit (VMTK) [23], where 3D surface model is generated by using various level set techniques. A volume can then created from the surface from which a mesh can be generated. This process is illustrated in Figure 1.2.3, where the mesh of a blood vessel extracted from the geometry is shown to the right. The final mesh is used as input in the FEniCS fluid flow solver.

## 1.3 Gender differences in the intracranial vasculature

In this section, we present an overview of a study recently published in [16] where it is shown that on average, women have larger shear stresses than men in two intracranial bifurcations.

#### 1.3.1 Background

Females are more likely to harbor intracranial aneurysms than men and, consequentially, more frequently get subarachnoid hemorrhage (SAH) [11, 5]. The reason is not known, but studies suggest an increased risk of aneurysm rupture after the age of fifty, in the postmenopausal years. This might indicate the influence of hormonal factors on the vessel wall. This hypothesis is supported by the reduced risk of SAH with increased parity. However, studies have failed to prove a decisive correlation between hormonal factors and the risk of SAH. Another hypothesis is that high values of wall shear stress may influence the initialization of aneurysms. With measurements of radii and angles of intracranial bifurcations available from a previous study in our group [12], we therefore wished to reanalyze the data and calculate the gender specific hemodynamic forces by numerical simulations.

#### 1.3.2 Method

Measurements of 49 patients were performed to obtain the geometries of the middle cerebral artery (MCA) and internal carotid artery (ICA) bifurcations. The averaged values were used to create one idealized bifurcation of the MCA and ICA for both females and males. The model basically consists of three cylinders connected with a smoothing at the interface to give a physiologically correct appearance.

Average gender specific blood flow velocity measurements from the ICA and MCA from [15] were used as inflow boundary conditions in the simulations. Table 1.2 summarizes the input values to the simulations, cf. [16]. At the outflows, we have applied a resistance boundary condition as described in Section 1.2.2.

#### 1.3.3 Results

Table 1.2 shows that there is a significant gender difference in the diameters for the MCA. For ICA, there are only statistical sex differences in the vessel size of the parent vessel and the smallest branch. CFD simulations shown both increased wall shear stress and a larger affected area in the female MCA (Figure 1.10) and ICA (Figure 1.11) bifurcations. The maximum wall shear stress in the MCA bifurcations was 33.17 Pa for females and 27.82 Pa for males. Similar results for ICA were 15.20 Pa for females and 10.10 Pa for males. The values are reflected by a higher pressure drop in the female than the male bifurcations (664 vs 502 Pa for MCA and 344 vs 202 Pa for ICA). For further discussion, see [16].

#### 1.3.4 Discussion

The above results are as expected from fluid mechanical reasoning, except from the peak values in the vicinity of the bifurcations. Even though the model is simple, the aim was to demonstrate a principle with a potentially important application, that is, that WSS may be of importance in the initialization and rupture of IA. Furthermore, the WSS computed based on the simulations suggest that women would have more aneurysms than men.

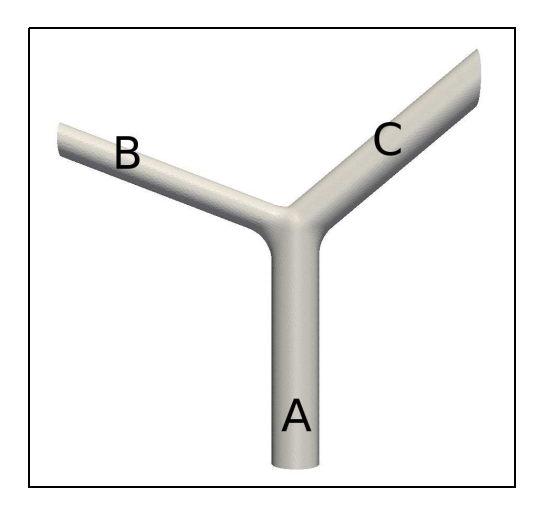


Figure 1.9: Idealized model of a bifurcation.

|               | Male MCA       | Female MCA     | Male ICA       | Female ICA     |
|---------------|----------------|----------------|----------------|----------------|
| α             | 49.7°          | 50.5°          | 62.8°          | 57.2°          |
| β             | $68.8^{\circ}$ | $72.5^{\circ}$ | $49.7^{\circ}$ | $50.5^{\circ}$ |
| A [mm]        | 2.63           | 2.42           | 3.86           | 3.45           |
| <i>B</i> [mm] | 2.44           | 2.04           | 2.71           | 2.49           |
| <i>C</i> [mm] | 1.74           | 1.56           | 2.13           | 1.85           |
| V [m/s]       | 0.68           | 0.74           | 0.34           | 0.42           |

Table 1.2: Summary of angles, diameters, and velocities used for the simulations. The parameters  $\alpha$  and  $\beta$  are the angles between the prolongation of the parent artery and the vessels C and B respectively.

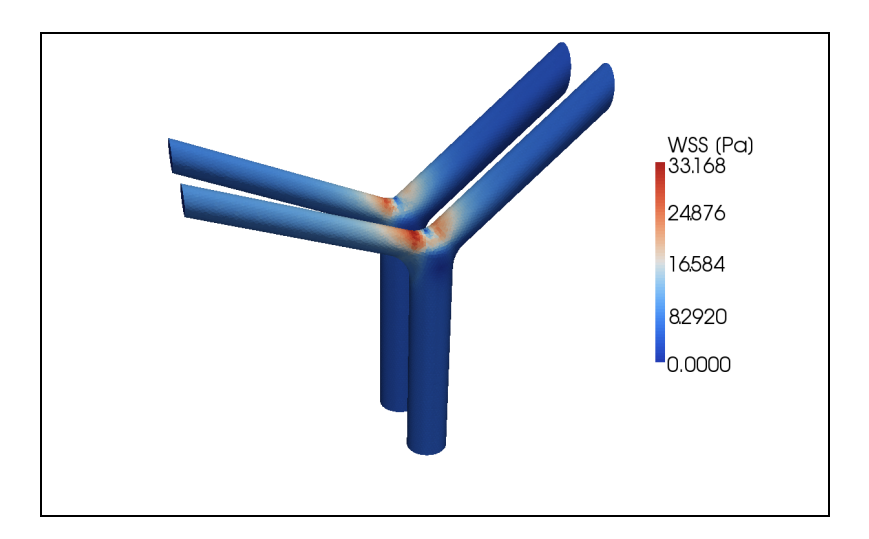


Figure 1.10: Resulting wall shear stress in the male and female MCA bifurcations. Female bifurcation in front.

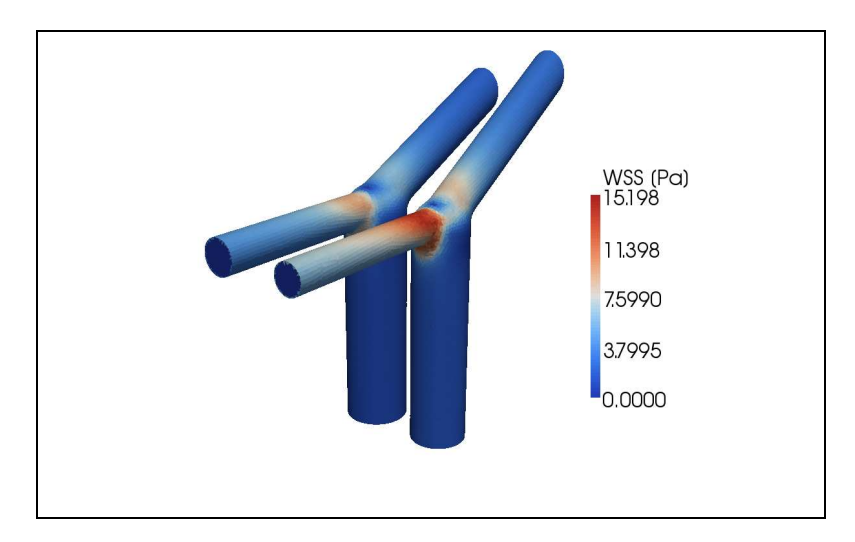


Figure 1.11: Resulting wall shear stress in the male and female ICA bifurcations. Female bifurcation in front.

### 1.4 CFD versus 4D PC MRA in an experimental canine aneurysm

In this study, see also [13], we quantitatively compared CFD, assuming Newtonian flow with rigid walls, with 4-Dimensional Phase Contrast Magnetic Resonance Angiography (4D PC MRA) techniques. The intention was both to verify the scientific techniques of going from a patient-specific model to CFD results and to understand and quantify the accuracy of the simplest possible flow model against state-of-the-art measurements.

4D PC MRA is a noninvasive technique to measure flow in the vasculature system. The image acquisition consists of a scan time of roughly 8 minutes. With an average heart rate of 101 beats per minute, the obtained images are an average over 808 heart cycles. There is naturally no guarantee for a constant heart beat in the canine, and this is of course error prone. However, in humans with larger diameters in the vasculatory system, errors have been shown to be of order 3-10+% in the pulmonary arteries [18, 6].

The resolution is coarse in both space and time, and computation of forces such as WSS might be difficult. In addition to this, there might be locations in the vascular system where stenosis/plaque is present and the quality of the 4D PC MRA might be poor. These are also often the spots of most interest. In many cases, there are also problems with the Velocity Encoding Sensitivity (VENC) which may produce noise and useless data. The VENC may be adjusted to capture a velocity within a specific range. However, less accurate data is obtained for a wide VENC and vice versa.

#### 1.4.1 MRI

To test the above mentioned techniques in a complex case, our collaborators at Wisconsin Institutes for Medical Research [26] created an artificial saccular aneurysm in a carotid bifurcation of a canine according to [10]. The inlet diameter was 3.2mm, the height 9.4mm, the width 4.3mm, the volume 254.3mm<sup>3</sup>, the ostium area 17.10mm<sup>2</sup>, and the aspect ratio 2.18, where the aspect ratio is defined as the ratio between the aneurysm height and the neck width.

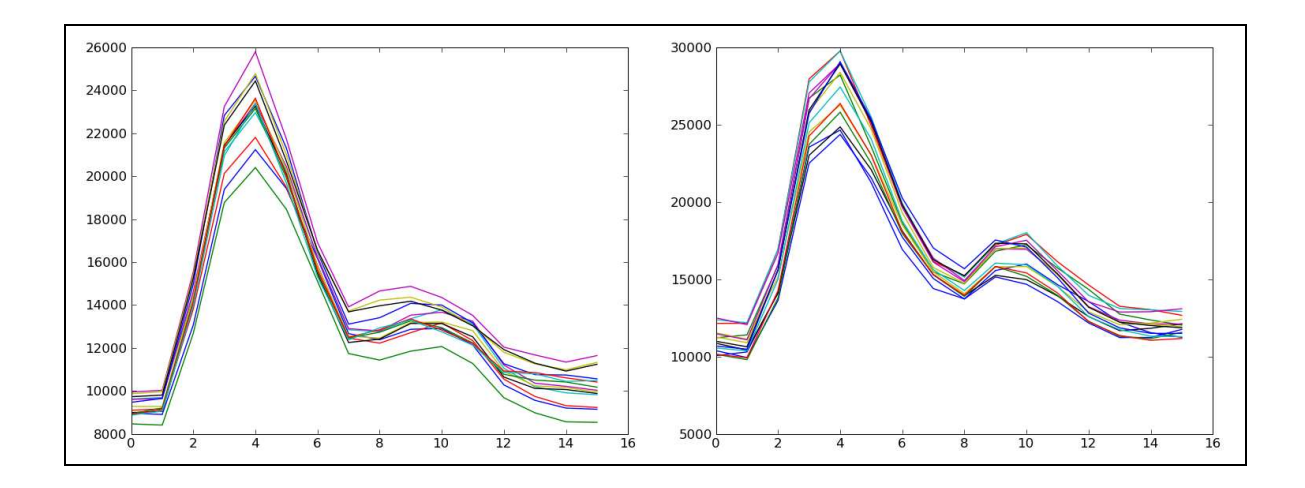


Figure 1.12: Measured differences in mass at inlet (left) and outlet (right) in a canine. The x-axis shows the time step number.

Three weeks after the artificial aneurysm was created, the canine was anesthetized and subjected to 4D PC MRA imaging studies, that is, the velocity measurements were performed. The velocity measurements are shown in Figure 1.12 where each solid line represents the sum of velocities at different cross sections of the inlet and outlet arteries. The picture to the left in Figure 1.12 shows the sum of velocities at the inlet, which is one artery, while the picture to the right show both the arteries where the outflow is. For a more thorough description, we refer to [13]. To get higher resolution images (of the vasculature only and not flow measurements), the canine underwent 3D-DSA within 24 hours. The coarse data obtained from 4D PC MRA is shown in Figure 1.13.

#### 1.4.2 CFD

The geometry was produced according to the procedure described in Section 1.2.3. We solved the incompressible Navier–Stokes equations using an incremental pressure correction scheme as described in Chapter [kvs-1]. We used first order elements for both velocity and pressure, simulated over four heart beats, and obtained the results from the last cycle. The CFL number is a dimensionless number that describes the temporal resolution relative to the grid spacing. With a CFL number of roughly ten, the number of time steps were 696 per cardiac cycle. As inflow boundary conditions, we used an average value from the five lower most voxels in the *z*-direction. For the outflow, we applied a resistance boundary condition as described in section 1.2.2. The inflow was chosen according to Figure 1.14 and Figure 1.15.

Figure 1.14 shows how the values in Figure 1.12 are returned as a spline function. The factor (133.0/256)\*\*-2 scales the voxel size to the matrix size, so that the focus of the image corresponds to the actual size in millimeters, and returns a value for the velocity. The t variable is the end time, and the scalar 0.037 is the equally spaced time steps of where measurements for v were made.

In Figure 1.15, a call is made to generate a spline representation of the velocity in time by calling makeIC(). Then, in eval\_data, n is the outward facing facet normal and t is the time.

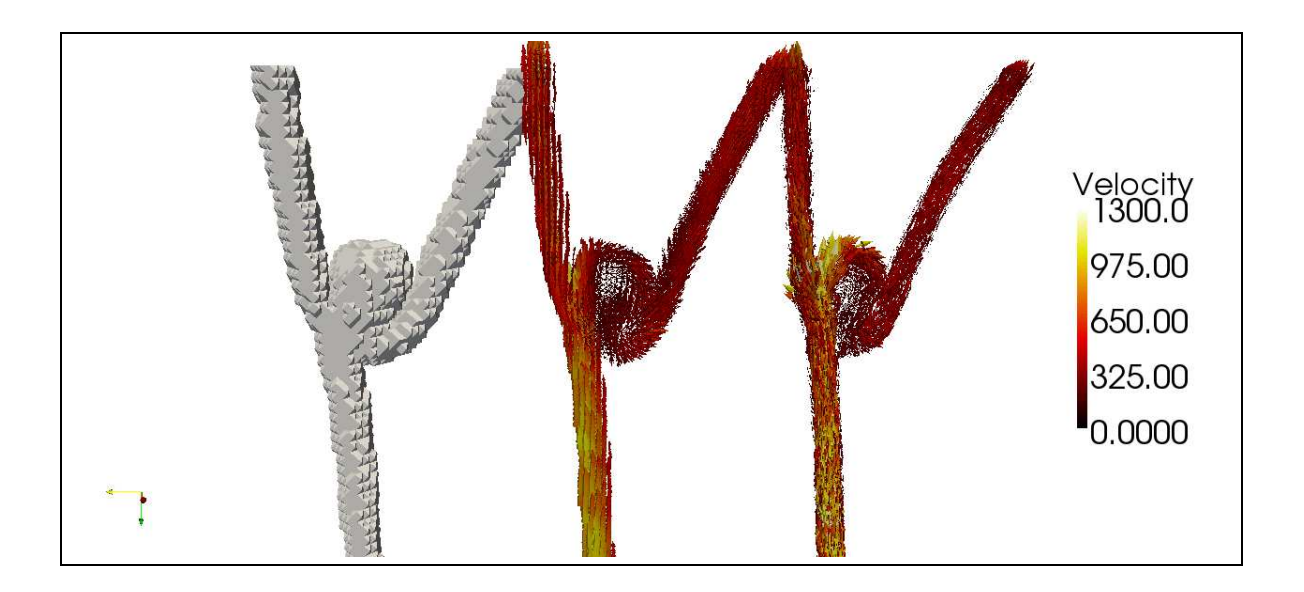


Figure 1.13: Figure showing resolution of data points where velocity measurements are made (left), velocity measurements from 4D PC MRA (middle), and CFD simulations (right).

Figure 1.14: Measured values used for spline representation for the inflow.

```
class InflowBoundaryValue(Expression):
   def init(self, problem=None, side=None):
       self.problem = problem
       self.side=side
       self.bc_func, self.t_period = makeIC()
   def eval_data(self, values, data):
       n = data.cell().normal(data.facet())
       t = self.problem.t
       val = splev(t - int(t/self.t_period)*self.t_period, self.bc_func)
       values[0] = -n.x()*val
       values[1] = -n.y()*val
       values[2] = -n.z()*val
   def rank(self):
       return 1
   def dim(self):
       return 3
```

Figure 1.15: Calculation of inflow boundary value for velocity.

The variable val is a spline evaluation such that the pulse goes in a continued cycle as time exceeds one heart beat. Finally, each component of the velocity vector, e.g., values[0], is given the component-wise negative value of n (to create a flow going into the domain) times the velocity value corresponding to the current time.

#### 1.4.3 Results

The resulting velocity field from 4D PC MRA and CFD calculations during peak systole are shown in Figure 1.13, and illustrates an overall good agreement between CFD and 4D PC MRA. For both canines (second one not included here), we obtained a similarity of more than 70% with respect to the velocity but only 22-31% similarity with respect to the WSS. For further details, we refer to [13].

#### 1.4.4 Discussion

The reason for using the average values of the five lower most cross sections as inflow is that given the resolution of the 4D PC MRA, each level of voxels is not necessarily mass conserving. As seen in Figure 1.12, the sum of mass in a plane may vary by as much as 20% between the different sections. It is also clearly visible in this figure that peak systole appears at time step four in both left (inflow) and right (outflow) image of the figure, but the "bump" at mid deceleration has shifted from time step seven at the inflow to eight at the outflow. This is a visualization of the so-called Windkessel effect, which may be captured using a fluid structure interaction model. This effect is also visible as the variation of how much the lines are spread vertically through the heart cycle.

A limitation of the current study is that the results should not be interpreted as physiologically correct since the technique consists of cutting off one of the ICAs and creating an artificial bifurcation (and aneurysm) by moving the rest of the vessel over to the other ICA. This means that one of the ICAs supply both left and right sides of the canine brain.

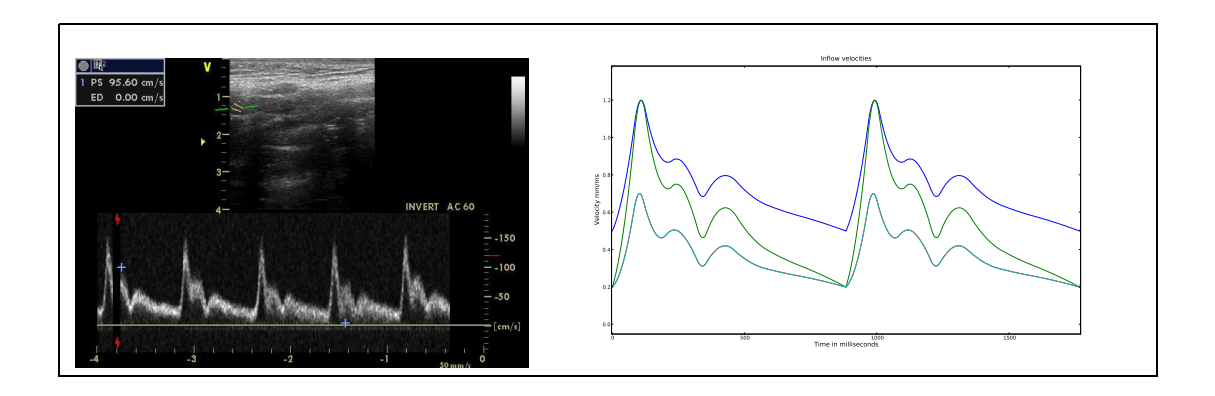


Figure 1.16: Inflow velocities used for simulation of blood flow in patient-specific Circle of Willis. Screenshot from TCD machine on left hand side with the artery on top and waveform on bottom. Implemented values to the right.

In the 4D PC MRA measurements at the left side of the parent artery in Figure 1.13, there are no boundary layers due to isotropic voxels, and the colors appear brighter since high velocities are possible close to the wall. The CFD simulations have short arrows at the same location indicating that the boundary layer has been resolved and we get lower velocities. This is an obvious drawback with the 4D PC MRA. Thus, we get a good agreement with the velocity measurements, but poor agreement for computed wall shear stresses. The reason for this is believed to be the poor spatial resolution of the 4D PC MRA data. For a more thorough description, we refer to [13].

Each method has its own strength and weaknesses. While 4D PC MRA is fast, cheap, and harmless, it uses average values over a voxel volume and fails to correctly compute WSS, recirculation zones, and possible turbulent structures. 4D PC MRA also fails at providing values where the VENC is out of focus or in the presence of a stenosis. Similarly, CFD is expensive but may provide accurate computations of WSS over the entire domain.

Combined, the two methods may give a better understanding of the importance of boundary conditions, whether or not fluid structure interaction is of importance, and possible pit-falls using the different methods. A first natural extension of this study may be to describe blood as a non-Newtonian fluid to determine whether or not non-Newtonian effects are of importance.

## 1.5 Patient-specific Circle of Willis

#### 1.5.1 Background

In a study performed in collaboration with doctors from the Neuroradiology department at Rikshospitalet University Hospital in Oslo [21], we wanted to investigate whether we are able to reproduce velocities in a full Circle of Willis with measurements at the inflow and compare with measurements at the outflow using resistance boundary conditions from the literature [1, 24]. Such an evaluation or verification of boundary conditions is essential, before proceeding with more sophisticated problems related to the entire intracranial vasculature.

```
for i in (6,7,8,9,10,11,12,13):
    g = OutflowBoundaryValue()
    g.init(self, i)
    self.gps.append(g)
    bc = DirichletBC(Q, g, self.sub_domains, i)
    g.current_t = 0
    self.gps.append(g)
    bcp.append(bc)
```

Figure 1.17: Calculation of resistance outflow boundary conditions for the pressure in the patient-specific CoW.

#### 1.5.2 Method

Transcranial Doppler (TCD) was performed at a healthy volunteer at rest. During the velocity recording, the average pulse was about 73 beats per minute. The velocity measurements of maximum and minimum values were used as input to the vessels that are the main suppliers of blood to the brain, that is, the ICAs and VAs. Figure 1.16 shows the resulting waveform (right) that was applied from the measurements (left). The figure shows the ICA velocities from the top with equal value at peak systole (120cm/s) and differing at end diastole (minimum 50cm/s in right ICA and 20 cm/s in left ICA). The lower most line has a different waveform and shows values for two superimposed VAs since they are equal. The vasculature, that is, the MRI data for this patient was already available from a previous study performed nine months earlier. The major vessels (ICA, MCA, PCA, ACA, VA, BA) were segmented as described in Section 1.2.3. The simulations were performed on meshes with three boundary layers where the number of cells were approximately 400,000, 900,000, and 2,600,000. We used P1-P1 elements and an incremental pressure correction scheme with Adams-Bashford implicit convection and Crank-Nicolson diffusion to solve the incompressible Navier-Stokes equations. The resolution in time was 3532 time steps per heart beat on the coarsest mesh.

Figure 1.17 shows how the outflow boundary conditions are set. The numbers 6 to 13 refer to the labels for the different outlets. For each outlet, the class OutflowBoundaryValue() is called, which returns a value for the pressure. Finally, the specific outlet is applied to a list of boundary conditions used in the Navier–Stokes solver.

#### 1.5.3 Results

Based upon images obtained from TCD, we compare only one point in time, peak systole. Since there is a large difference in the sum of inflow areas and the outflow areas, we only consider the flow division between the arteries compared to measurements. Table 1.3 shows the measured and calculated velocities for the major arteries.

#### 1.5.4 Discussion

The results of the current study do not match very well with measured values. This may indicate that the type of boundary conditions applied here may not describe the peripheral resistance properly. However, there are many sources of error that must be considered. First,

| Artery | Left Measured | Left Computed | Right Measured | Right Computed |
|--------|---------------|---------------|----------------|----------------|
| MCA    | 70, 120       | 87            | 140,150        | 55             |
| ACA    | 200           | 100           | 90,100         | 65             |
| PCA    | 70,80         | 62            | 80             | 100            |

Table 1.3: Measured versus computed values for flow velocities [cm/s] in a patient-specific Circle of Willis at peak systole. The cells with two values refers to different measurements made with a 5 weeks difference in time.

```
def area(self, i):
    f = Constant(1)
    A = f*ds(i)
    a = assemble(A, exterior_facet_domains=self.sub_domains, mesh=self.mesh)
    return a
```

Figure 1.18: Calculation of the areas in sub domains.

TCD is difficult to perform and subject to errors. Personal communication with the neurora-diologist suggests errors at the scale of 20%. Second, we have no information on when peak systole appears in the different arteries. It seams reasonable that there is a small shift in time since the blood goes from the heart and through different arteries before it meets in CoW. At present, we have not been able to quantify this shift. Third, the velocity itself may differ at different times for various reasons. This is illustrated by the cells containing two values in Table 1.3, which refers to two measurements of the same vessel in the same person only 5 weeks apart.

It is also a great challenge to segment the complete CoW due to the great variations in diameters. This is clearly visible when performing an automatic segmentation where many of the smaller vessels disappear. It is known that the BA has approximately 50 tiny vessels that are clearly not present in Figure 1.19. The reason for this is that MRA measurements are based upon velocities, and hence the velocities in these vessels are too small to be captured. By calculating and summing up the in- and outflow areas using the code in Figure 1.18, we actually get an area difference of  $37.18mm^2 - 25.33mm^2 = 11.85mm^2$ . It is not known what the correct area should be.

The simulations also show that it might be a problematic to not include a large fraction of the parent artery when performing simulations on a smaller fraction of the vasculature. It is common to apply either a flat velocity profile or a Womersley profile upstream of the location of interest. This is clearly not the case as shown in Figure 1.20 where the flow is highly non-uniform.

#### Source code and data

The source code for this chapter can be found at www.fenics.org/to\_be\_decided/kvs-2. The solver builds on the code developed in Chapter [kvs-1]. We have also included velocities and anatomy from the MRA and the DSA data from the canine study. Finally, we include MR data for the patient-specific Circle of Willis and corresponding transcranial ultrasound images for the blood velocities.

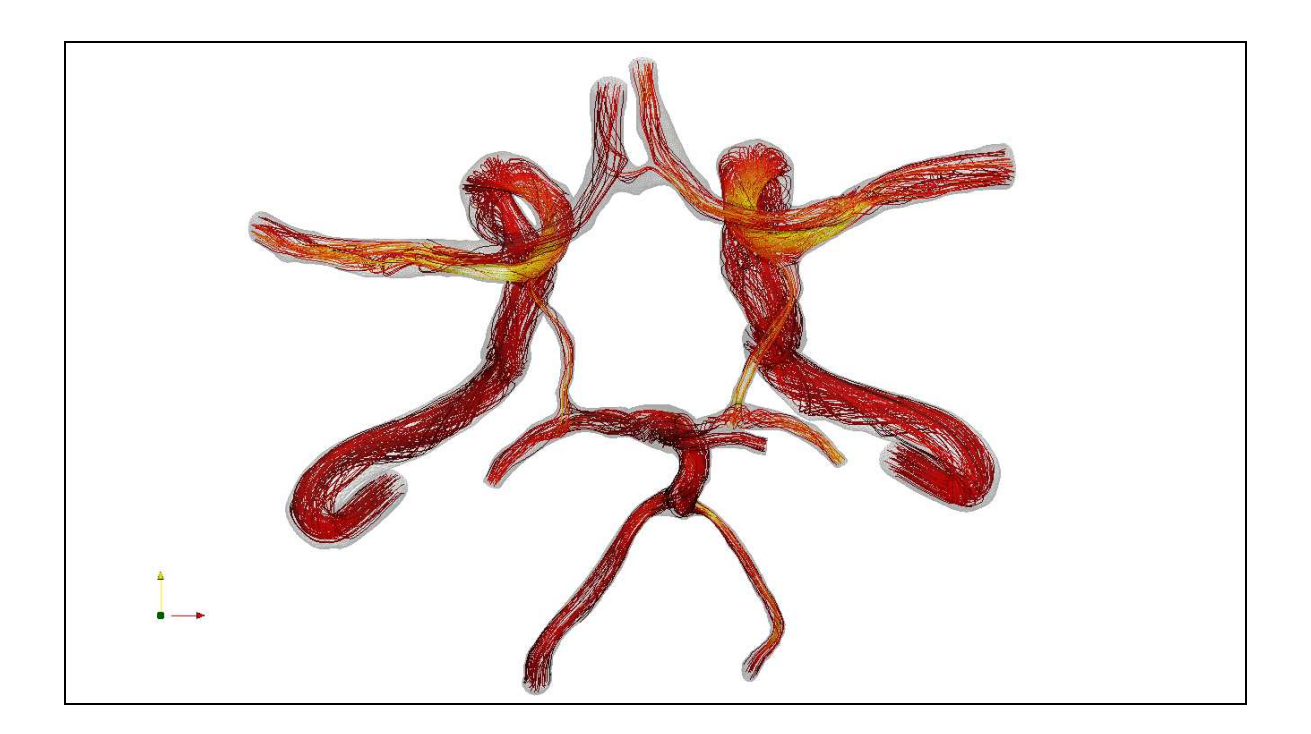


Figure 1.19: Patient-specific Circle of Willis.

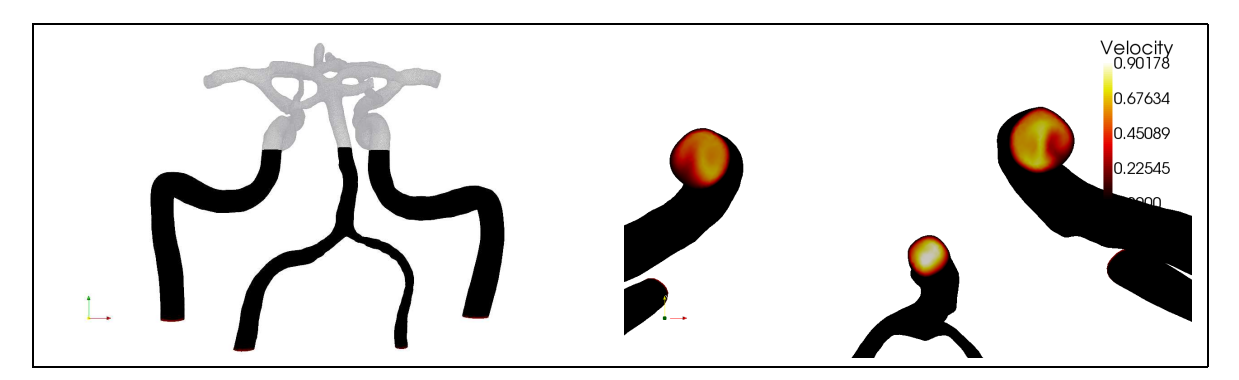


Figure 1.20: Left figure illustrating plane where figure at right is cut from. Right figure showing highly non-uniform flow in ICA.

## **Bibliography**

- [1] J. ALASTRUEY, K. PARKER, J. PEIRO, S. BYRD, AND S. SHERWIN, Modelling the circle of willis to assess the effects of anatomical variations and occlusions on cerebral flows, Journal of Biomechanics, 40 (2007), pp. 1794–1805.
- [2] L. BOUSSEL, V. RAYZ, C. MCCULLOCH, A. MARTIN, G. ACEVEDO-BOLTON, M. LAWTON, R. HIGASHIDA, W. S. SMITH, W. L. YOUNG, AND D. SALONER, Aneurysm Growth Occurs at Region of Low Wall Shear Stress: Patient-Specific Correlation of Hemodynamics and Growth in a Longitudinal Study, Stroke, 39 (2008), pp. 2997–3002.
- [3] J. R. CEBRAL, M. A. CASTRO, J. E. BURGESS, R. S. PERGOLIZZI, M. J. SHERIDAN, AND C. M. PUTMAN, Characterization of Cerebral Aneurysms for Assessing Risk of Rupture By Using Patient-Specific Computational Hemodynamics Models, AJNR Am J Neuroradiol, 26 (2005), pp. 2550–2559.
- [4] P. F. DAVIES, A. REMUZZI, E. J. GORDON, C. F. DEWEY, AND M. GIMBRONE, *Turbulent fluid shear stress induces vascular endothelial cell turnover in vitro*, Proc. Natl. Acad. Sci. USA, 83 (1986), pp. 2114–2117.
- [5] S. EDEN, W. MEURER, B. SANCHEZ, L. LISABETH, M. SMITH, D. BROWN, AND L. MORGENSTERN, Gender and ethnic differences in subarachnoid hemorrhage, Neurology, 71 (2008), pp. 731–735.
- [6] A. EVANS, F. IWAI, T. GRIST, H. SOSTMAN, L. HEDLUND, C. SPRITZER, R. NEGRO-VILAR, C. BEAM, AND N. PELC., Magnetic resonance imaging of blood flow with a phase subtraction technique. in vitro and in vivo validation., Investigative radiology, 28 (1993).
- [7] V. FEIGIN, Stroke epidemiology in the developing world, The Lancet, 365 (2005), pp. 2160–2161.
- [8] M. D. FORD, N. ALPERIN, S. H. LEE, D. W. HOLDSWORTH, AND D. A. STEINMAN, *Characterization of volumetric flow rate waveforms in the normal internal cartoid and vertebral arteries*, Physiological Measurement, 26 (2005), pp. 477–488.
- [9] Y. C. Fung, Biodynamics: Circulation, Springer-Verlag, 1984.
- [10] W. J. GERMAN AND S. P. W. BLACK, Cervical ligation for internal carotid aneurysms, Journal of Neurosurgery, 23 (1965), pp. 572–577. PMID: 5861140.
- [11] J. D. HUMPHREY, Cardiovascular Solid Mechanics, Springer, 2001.

- [12] T. INGEBRIGTSEN, M. MORGAN, K. FAULDER, L. INGEBRIGTSEN, T. SPARR, AND H. SCHIRMER, *Bifurcation geometry and the presence of cerebral artery aneurysms.*, J Neurosurg., 101 (2004), pp. 108–113.
- [13] J. JIANG, K. JOHNSON, K. VALEN-SENDSTAD, K.-A. MARDAL, O. WIEBEN, AND C. STROTHER, Flow characteristics in a canine aneurysm model: A comparison of 4-d accelerated phase-contrast mr measurements and computational fluid dynamics simulations (submitted), American Journal of Neuroradiology, (2010).
- [14] G. KONGABLE, G. LANZINO, T. GERMANSON, L. TRUSKOWSKI, W. ALVES, J. TORNER, AND N. KASSELL, *Gender-related differences in aneurysmal subarachnoid hemorrhage*, Journal of Neurosurgery, 84 (1996), pp. 43–48.
- [15] J. Krejza, P. Szydlik, D. S. Liebeskind, J. Kochanowicz, O. Bronov, Z. Mariak, and E. R. Melhem, *Age and Sex Variability and Normal Reference Values for the VM-CA/VICA Index*, AJNR Am J Neuroradiol, 26 (2005), pp. 730–735.
- [16] H. LINDEKLEIV, K. VALEN-SENDSTAD, M. F. MORGAN, K.-A. MARDAL, K. FAULDER, J. MAGNUS, K. WATERLOO, B. ROMNER, AND T. INGEBRIGTSEN, Sex differences in intracranial arterial bifurcations, Gender Medicine, (2010).
- [17] W. LONGSTRETH, L. NELSON, T. KOEPSELL, AND G. VAN BELLE, Subarachnoid hemorrhage and hormonal factors in women. a population-based case-control study, Ann Intern Med, 121 (1994), pp. 168–173.
- [18] J. LOTZ, C. MEIER, A. LEPPERT, AND M. GALANSKI, Cardiovascular Flow Measurement with Phase-Contrast MR Imaging: Basic Facts and Implementation1, Radiographics, 22 (2002), pp. 651–671.
- [19] C. MHURCHU, C. ANDERSON, K. JAMROZIK, G. HANKEY, AND D. DUNBABIN, Hormonal factors and risk of aneurysmal subarachnoid hemorrhage: An international population-based, case-control study, Stroke, 32 (2001), pp. 606–612.
- [20] C. J. MURRAY AND A. D. LOPEZ, Alternative projections of mortality and disability by cause 1990-2020: Global burden of disease study, The Lancet, 349 (1997), pp. 1498 1504.
- [21] Rikshospitalet. www.rikshospitalet.no/.
- [22] W. E. Stehbens, Ultrastructure of Aneurysms, Arch Neurol, 32 (1975), pp. 798–807.
- [23] Vascular Modeling Toolkit. http://vmtk.org/.
- [24] I. E. VIGNON-CLEMENTEL, C. A. FIGUEROA, K. E. JANSEN, AND C. A. TAYLOR, Outflow boundary conditions for three-dimensional finite element modeling of blood flow and pressure in arteries, Computer Methods in Applied Mechanics and Engineering, 195 (2006), pp. 3776 3796. Absorbing Boundary Conditions.
- [25] B. Weir, *Unruptured intracranial aneurysms: a review*, Journal of Neurosurgery, 96 (2002), pp. 3–42.
- [26] Wisconsin Institutes for Medical Research (WIMR) at the University of Wisconsin School of Medicine and Public Health in Madison. www.med.wisc.edu/wimr/.